Reversible potassium-ion alloying storage in crystalline silicene

Yuanhe Sun [a,b,c], Yuanxin Zhao [a,b], Zhaofeng Liang [a,b], Han Lin [d,*], Zhiguo Ren [a,b], Zeying Yao [a,b,c], Yaru Yin [e], Ping Huai [a,b], Ke Yang [a,b], Jinyou Lin [a,b], Yaobo Huang [a,b], Wen Wen [a,b], Xiaolong Li [a,b], Renzhong Tai [a,b,*], Daming Zhu [a,b,*]

[a] *Shanghai Institute of Applied Physics, Chinese Academy of Sciences, Shanghai 201800, PR China*
[b] *Shanghai Synchrotron Radiation Facility, Shanghai Advanced Research Institute, Chinese Academy of Sciences, Shanghai 201204, PR China*
[c] *University of Chinese Academy of Sciences, Beijing 100049, PR China*
[d] *Shanghai Institute of Ceramics, Chinese Academy of Sciences, Shanghai 201899, PR China*
[e] *Centre for Transformative Science, ShanghaiTech University, Shanghai 201210, PR China*

ARTICLE INFO

ABSTRACT

Silicon has been recognized as one of the most appealing alloying anode materials for lithium/sodium-ion storage. However, the K-Si alloying reaction is still missing in potassium-ion batteries produced so far, even though the theoretical phase diagram allows the existence of corresponding products. Herein, we synthesize crystalline silicene from Zintl phase $CaSi_2$ and demonstrate that potassium-ions can be inserted/extracted efficiently in it with enhanced cycle stability (without capacity fading over 3000 cycles in silicene//K battery with Coulombic efficiency remains above 99.4 %). Contrary to established perceptions of "inert silicon", the reversible kinetics-controlled K-Si phase transition occurring in silicene is illustrated by in situ synchrotron X-ray diffraction, and enables the formation of KSi as the dominant discharged product realizing a reliable reversible potassiation storage capacity of 180.1 mA h g^{-1}. The versatile alloying electrochemistry of silicon observed here is expected to spur the development of durable potassium-ion batteries.

1. Introduction

The rapidly increasing demand for the renewable energy resources calls for sustainable energy storage devices and promoted the vigorous development of alkaline-ion batteries (Li, Na, and K).[1–3] The dominant lithium-ion batteries (LIBs) are pervasive across most types of consumer electronics such as electric vehicles and portable electronics; besides, sodium-ion batteries (NIBs) and potassium-ion batteries (KIBs) provided more cost-effective choices for large-area formats benefiting from the high abundance of resources, jointly facing the challenge of investigating suitable electrode materials for boosting facile ion storage. [4–6] Silicon, which is the main non-gas element in the crust, has revealed as promising anode candidates for LIBs to replace traditional graphite electrodes with high theoretical specific capacity, but failed in KIBs owing to the currently considered inert reactivity.[7] On the one hand, like silicon suffers from the severe deformation caused by the intercalation of lithium-ions in LIBs, potassium-ions with larger ionic radius as 1.38 Å will cause more seriously huge distortions of host electrode materials during the insertion/extraction processes and lead to

irreversible structural degradation of the electrode upon cycling.[8] On the other hand, Sultana et al. experimentally confirmed that the reversible capacity was almost invisible in the commercial crystalline silicon (c-silicon) powder/graphene anode and demonstrated the absence of K-Si alloying products in the full-discharged product.[9] To date, although the reported theoretical calculations illustrated the existence of possible K-Si alloying products (such as KSi or $KSi_{5.75}$), reversible electrochemical potassium-ion storage in silicon has not been activated.[10]

In general, the possible potassiation products of silicon such as KSi are classified as the so-called Zintl phase, silicon atoms forming isolated $[Si_4]^{4-}$ tetrahedra and the octet rule is completed by one electron from the cation.[11] Similarly, the sodiation products of Si such as NaSi and calciation products such as $CaSi_2$ also obeys Zintl-Klemm formalism. [12] An intuitive idea is, considering the similar robust structure and abundant reaction sites, the silicene derived from $CaSi_2$ is expected to be beneficial to alloying with potassium-ions and ignite the performance of silicon, especially c-silicon in KIBs.[13] Moreover, as Xu. et al. recently reported, c-silicon nanoparticles with high specific surface area are used

---

as the anode of NIB, activate a reversible Na-Si alloying reaction and generate $Na_{1-x}Si$ species, which provide 248 mA h g^{-1} at 20 mA g^{-1} after 100 cycles.[14] The flexible monolayer nanosheet structure of silicene also possesses increased reaction area with shortened ion transport pathway, hasten interfacial charge transfer, and is conducive to maintaining structural integrity and achieving stable cyclability. Therefore, it is still urgent to exploit compatible silicene electrode and investigate the corresponding energy storage mechanism in KIBs.

Herein, free-standing crystalline silicene (c-silicene) nanosheets are synthesized from Zintl phase $CaSi_2$ and used as the first reversible c-silicon anode for KIBs with an extended cycle life. In situ synchrotron X-ray diffraction measurements (SXRD) confirm the reversible kinetics-controlled K-Si phase transition, and the formation of the KSi as the dominant discharge alloying product is further illustrated by multiple characterization techniques. The proposed c-silicene//K battery demonstrates a reliable reversible potassiation storage capacity of 180.1 mA h g^{-1} at 10 mA g^{-1} suggesting highly reversible reaction. Benefiting from the monolayer morphology and the robust structure of c-silicene, cycling stability over 3000 cycles at 500 mA g^{-1} with the Coulombic efficiency remains above 99.4 % is achieved without observable capacity attenuation, towards the superior silicon anodes with ultra-stable cycling performance.

2. Experimental section

2.1. Raw materials

Calcium silicide ($CaSi_2$, tech-95, 95%, powder, Gelest), iodine (I_2, 99.99%, Sigma-Aldrich), 1-methyl-2-pyrrolidinone (NMP, anhydrous, 98%, Sigma-Aldrich), and acetonitrile (CH_3CN, anhydrous, 99.8%, Sigma-Aldrich) were obtained and used as received.

2.2. Materials synthesis

Briefly, c-silicene was prepared as follows. First, 575 mg of the $CaSi_2$ precursor and 1524 mg of the I_2 powder precursor (molar ratio = 1:1) were immersed and stirred in 160 mL of anhydrous acetonitrile (CH_3CN). The reaction process continued at room temperature for 2 weeks under Ar atmosphere protection. After centrifugation and washing with anhydrous acetonitrile three times, the precipitate underwent a thermo-enabled expansion process (heated to 380 °C) and was subsequently immersed in liquid N_2 until the liquid N_2 completely gasified (quenched to −196 °C). Finally, the samples were stored in NMP.

2.3. Materials characterization

The morphology, composition, and structure of c-silicene were studied by scanning electron microscopy (SEM, Carl Zeiss Gemini SEM 300), X-ray photoelectron spectroscopy (XPS, Kratos Analytical Axis UltraDLD) and transmission electron microscopy (TEM, JEM-2100 and JEM-2100F). A Raman spectrometer (RENISHAW inVia Basis; 532 nm) was used for analyzing the layered structure. Atomic force microscopy (AFM, CSPM-5500) was used to assess the height of c-silicene.

2.4. Electrochemical measurements

The electrochemical performance of c-silicene was tested via CR2025 coin-type cells from 0.01 to 3.0 V. The c-silicene electrode was prepared by mixing c-silicene, carbon black, and carboxymethyl cellulose (CMC) sodium salt in a mass ratio of 7:2:1. The mixture was uniformly coated on the copper foil and dried under vacuum overnight. The dried composite electrodes were cut into round pieces with a diameter of 0.6 cm by a disc cutter machine, typical load is 1–2 mg cm^{-2}. To prepare the electrolyte (battery grade, Ningbo Shanshan Co., Ltd.) for the KIBs, 3 M KFSI was prepared in dimethyl ether and used for the potassium

reaction. The cells were assembled in an argon-filled glove box. In the full KIB, Prussian blue analogue is used as the cathode. To prepare Prussian blue, 0.3244 g $FeCl_3$ and 0.3683 g $K_4Fe(CN)_6$ were separately dissolved in 40.0 and 160.0 mL of deionized water, and two solutions are slowly mixed evenly. Stir the mixture for two hours and then let it stand overnight at room temperature. The precipitate in the beaker was centrifuged and washed thoroughly, and dried at 100 °C in vacuum oven for 24 h to obtain Prussian blue. In a typical cathode preparation process, active material, carbon black (CB), and carboxymethyl cellulose (CMC) sodium salt were ground and mixed completely in a mass ratio of 8:1:1, and coated on aluminum foil. Then the electrode was dried in a vacuum oven at 60 °C for more than 24 h. Finally, $K_{0.22}Fe(Fe(CN)_6)$ was discharged to 2.0 V in the half-cell to obtain potassium-rich cathode. The mass ratio of cathode to anode is 6:1, which means that the cathode-to-anode electrode capacity ratio is approximately 3:1. The electrolyte is the same as the half-cell, and the c-silicene cathode is pre-activated. The cycle test voltage range of the full battery is set to 1.2–3.2 V. The cycling performances of c-silicene were determined at various rates with a LAND CT2001A battery test system. The cyclic voltammetry (CV) test was performed with a CHI 760E (Chenhua Instrument Company, Shanghai, China) electrochemical workstation.

2.5. In situ synchrotron Radiation-Based X-ray diffraction experiment

In situ XRD experiments were performed with an X-ray wavelength of 0.693 Å in beamline BL02U2 of the Shanghai Synchrotron Radiation Facility (SSRF). Moreover, the in situ XRD study was carried out using a special coin cell. There were two observation holes with a radius of ∼ 2 mm in the middle of both the cathode and anode sides, guaranteeing that X-rays could penetrate through the active materials during cycling. The observation hole of the specially made in situ cell was sealed by polyimide tape. The electrochemical current density used for the in situ experiment was 100 mA g^{-1}.

3. Results and discussion

Briefly, c-silicene was formed via the liquid oxidation and exfoliation of $CaSi_2$ (Fig. 1a). $CaSi_2$ has alternating stacked $(Ca^{2+})_n$ and $(Si_{2n})^{2n-}$ layers; thus, silicene can be expected to peel off when the $(Ca^{2+})_n$ layers are oxidized by I_2 and dissolved. The as-reacted c-silicene sheet powder display a high degree of crystallization with X-ray diffraction (XRD), and all the diffraction peaks of silicene sheets can be well indexed (JCPDS No. 27–1402) (Fig. 1b).[15] The scanning electron microscopy (SEM) images of the obtained c-silicene exhibit a stacked layer structure (Fig. 1c), which indicate that the product is adequately exfoliated (Fig. S1a). Energy dispersive X-ray spectroscopy (EDS) mapping shows almost invisible distribution of calcium in c-silicene, confirming the complete transition from $CaSi_2$ to c-silicene. The product was placed in deionized water for further ultrasonic exfoliation to obtain self-supported and dispersed ultra-thin silicene nanosheets. The atomic force microscopy (AFM) observation of dispersed c-silicene shows a uniform contrast with an average chip size of 3–5 μm and thickness of ∼ 0.65 nm, i.e., monolayer silicene (Fig. 1d, Fig. S2). The SEM image of c-silicene (Fig. S1b) provides similar evidence for the lamellar morphology. Considering its application in potassium-ion energy storage (Fig. 1e), monolayer c-silicene provides sufficient ion storage space and surface reaction sites and is expected to promote the occurrence of electrochemical reactions.

To investigate the morphology and detailed structure of c-silicene, transmission electron microscopy (TEM) was further conducted. Fig. 2a illustrates that c-silicene possesses a two-dimensional transparent texture and smooth morphology (Fig. S3), suggesting the integrity of $(Si_{2n})^{2n-}$ layers upon the I_2 treatment and stripping process. Moreover, a weak oxygen response is shown in the element mapping images compared with the obvious and uniform distribution of silicon, indicating the low degree of oxidation of c-silicene, and the observed oxygen
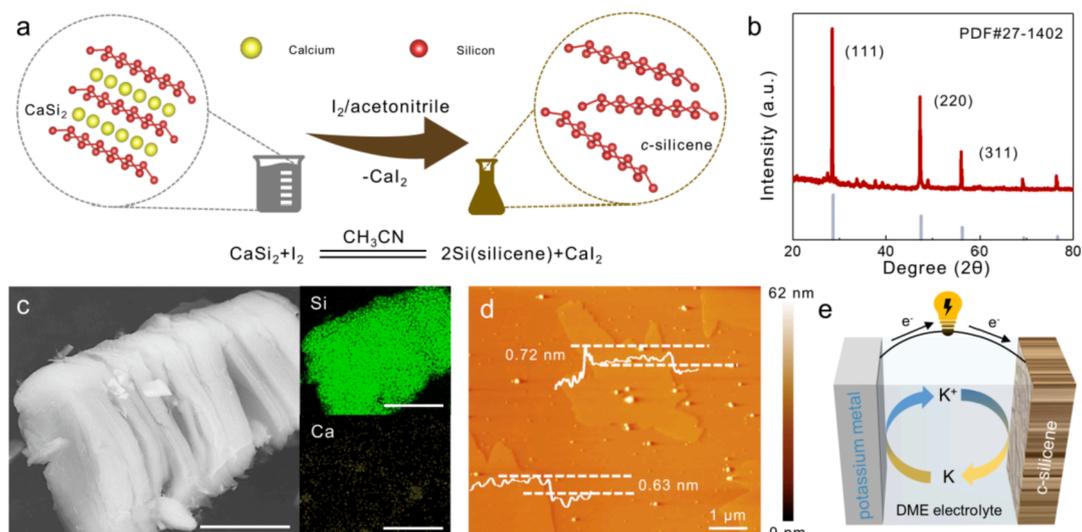
Fig. 1. (a) Schematic diagram showing the synthesis process of c-silicene. (b) XRD patterns of c-silicene. (c) SEM image, and corresponding Si and Ca elemental mappings of c-silicene. The scale bars is 5 μm. (d) AFM image of c-silicene with a monolayer morphology. (e) Schematic diagram of potassium-ion energy storage assembled with silicene as electrode.
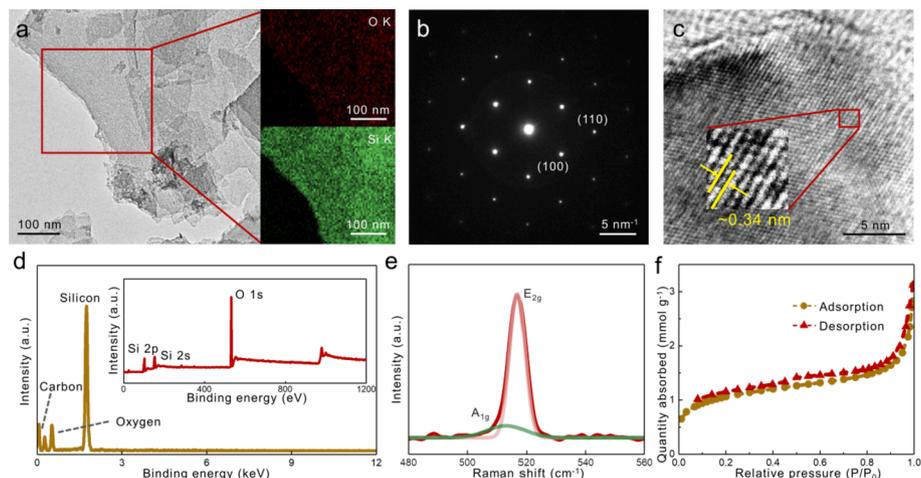
Fig. 2. (a) TEM images and the corresponding O and Si elemental mapping images of c-silicene. (b) The corresponding SAED pattern and (c) HRTEM images of c-silicene. (d) EDS spectrum and XPS survey spectrum (inserted) of c-silicene. (e) Raman spectrum of c-silicene. (f) Adsorption and desorption curves of c-silicene.

distribution can be attributed to the absorption behaviour of the silicene surface. The selective area electron diffraction (SAED) pattern was also measured (Fig. 2b), further verifying the single crystal morphology of the inherited silicon framework. As shown in Fig. 2c, the lattice of silicon atoms with interplanar spaces of ∼ 3.4 Å for the (1 0 0) plane is shown in the high-resolution TEM (HRTEM) image, which also reveals the well-crystallized feature of c-silicene. X-ray photoelectron spectroscopy (XPS) measurements and EDS analysis are shown in Fig. 2d. The XPS spectrum shows the obvious signals at ∼ 103 and ∼ 153 eV which can be attributed to Si 2p and Si 2 s respectively. It can be noted that although the O 1 s signal from the surface at ∼ 532 eV was observed, only a few oxygen elements are detected in EDS spectrum because of the deeper detection depth than XPS measurements. Moreover, the elemental composition analysis of the EDS spectrum declares a silicon content of up to 92%, as well as a small amount of carbon (5.6%) and oxygen (1.9%) signals (Table S1). Therefore, the O 1 s peak measured by XPS is attributed to the adsorption of the broad surface. The fine Si 2p spectrum can be dissociated into peaks at 99.0 eV and 102.4 eV, which can be attributed to Si-Si bonding and SiO_x/Si-OH species, respectively (Fig. S4).[16] Raman analysis was used to further determine the structure of c-silicene. The complete Raman spectrum shown in Fig. 2e agrees

with the typical Raman spectrum of buckled silicene and can be attributed to the out-of-plane vibrational mode (A_{1g}) and in-plane vibrational mode (E_{2g}). The vertical buckling is responsible for the A_{1g} breathing mode, which generates the asymmetric shoulder of the peak; the sharp and intense E_{2g} peak centred at 517 cm^{-1} is induced by the symmetric stretching of sp^2 Si-Si bonds, confirming the well-maintained structure of silicene and further indicates complete exfoliation.[17,18] The Brunauer–Emmett–Teller (BET) surface area of c-silicene was evaluated to be 78.7 m^2 g^{-1}, as shown in Fig. 2f, implying abundant reaction sites for potassium-ion storage given the application of anodes in KIBs.

To this day, crystalline silicon is still considered "inert" to potassium-ions, which means that Si//K alloys cannot be electrochemically formed in traditional silicon anode. Therefore, to elucidate the possible ignited electrochemical potassiation/depotassiation mechanism, a K/c-silicene cell was assembled and further performed by in situ SXRD. As can be seen in Fig. 3a-c, the periodic dis/reappearance of diffraction peaks suggests the occurrence of reversible phase changes in the K//c-silicene cell. In the stages of potassiation, the peaks located at 32.28° attributed to d (3 3 1) of c-silicene gradually weaken during the discharge process (Fig. 3b), and a strong peak at 21.28° appears when discharging to ∼ 0.3 V, indicating a conversion reaction. This observation demonstrates the
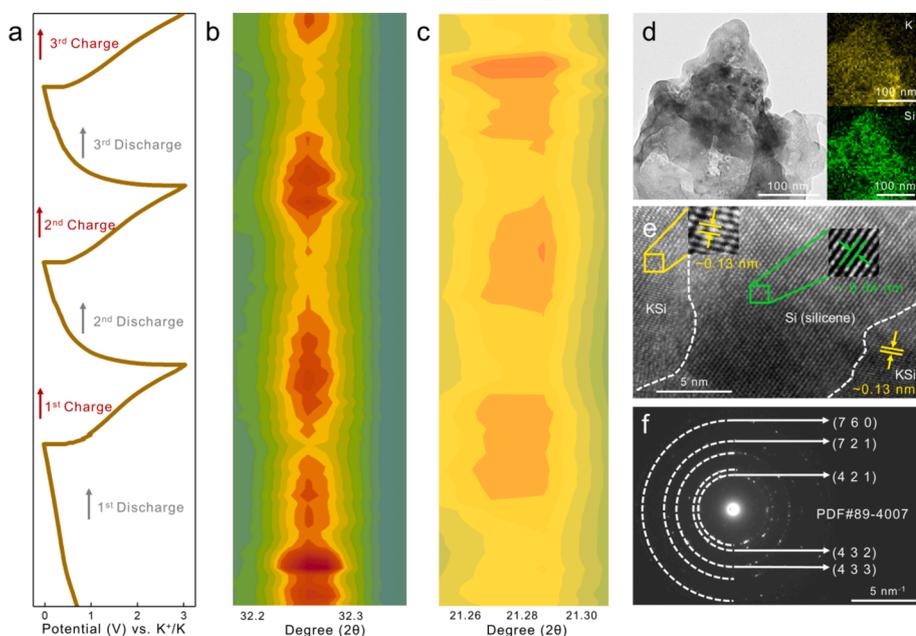
Fig. 3. In situ SXRD and TEM measurements. (a) Galvanostatic charge–discharge curves between 0.01 and 3.0 V at 100 mA g^{-1} during the in situ observation. (b) In situ SXRD patterns of c-silicene during the discharge/charge scan. (c) In situ SXRD patterns of the discharging product during the discharge/charge scan. (d) TEM images and the corresponding K and Si elemental mapping images of c-silicene. (e) Corresponding HRTEM images of c-silicene and KSi. (f) Corresponding SAED pattern of KSi.

formation of new species which can be attributed to the Bragg diffraction of the (6 3 0) crystal plane of KSi. Subsequently, when further discharging, the diffraction peaks attributed to silicon continues to weaken, and strengthens again during the following charging process. In contrast, the new species generated during the discharge process with the peak located at 21.28° fades gradually, and further reach the weakest when charging to ~ 2.2 V, which confirms the existence of reversible potassiation/depotassiation process within working potential range. Furthermore, the full-discharge products were further studied to confirm the alloying process. As shown in Fig. 3d, TEM was used to check the potassiation products in proposed cell, and the corresponding elemental mapping indicates the uniform distribution of potassium. It is worth noting that in the HRTEM analysis of the as-prepared full-discharged products, the lattice fringes of two widths are revealed in Fig. 3e together, which can be calculated as ~ 0.34 nm and ~ 0.13 nm respectively. As mentioned above, the lattice with ~ 0.34 nm lattice spacing is considered to be belong to c-silicene as (1 0 0) plane, consistent with original anode. In addition, the emerging lattice with ~ 0.13 nm width is incompatible with existing lattice spacing of c-silicene, and can be possibly attributed to the (7 2 1) plane of KSi (JCPDS No. 89–2863).[19] The SAED pattern of the selected potassiation product

shown in Fig. 3f is further calculated, and the corresponding facet index is obtained. The brightest diffraction ring is mapped as d = 0.278 nm, corresponding to the (4 2 1) crystal plane, while the ring of d = 0.238 nm is also calculated and corresponds to the (4 3 2) crystal plane of KSi. Although affected by contrast and background, other diffraction rings that can be identified are also marked and corresponding to KSi crystal. Thus far, the reversible reaction of c-Si electrode was successfully ignited in KIBs, and the above analysis illustrates the alloying reaction mechanism of the K//c-silicene battery and the existence of KSi during the electrochemical processes.

In addition, the full-discharge products were further studied to confirm the unique alloying process by SEM-EDS and XPS. The EDS spectrum of the proposed electrode (Fig. S5) shows that the new spectral line assigned to K K$_\alpha$ appears at E = 3.31 keV, which confirms the significant potassiation. SEM analyses were carried out to provide more intuitive visual evidence, and the cross-section and surface of the electrode are measured and displayed in Fig. 4a and Fig. S6 respectively, indicating the uniform distribution of potassium on the whole electrode. XPS was performed to examine the valence changes of silicon and potassium. As shown in Fig. S7, compared with those of the original c-silicene, the K 2p and K 2 s peaks appear at 293 eV and 377 eV, and can
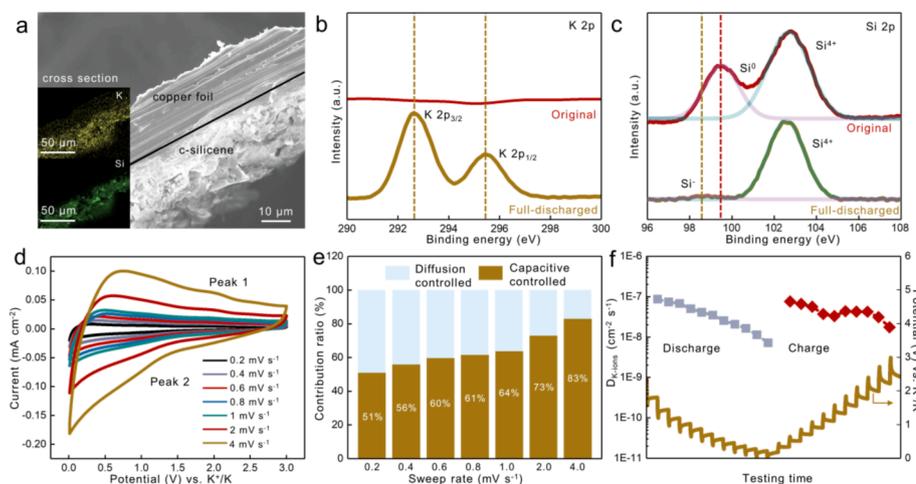
Fig. 4. Full-discharged product analysis and kinetic measurement. (a) SEM image of the cross-section of a full-discharged c-silicene electrode with the corresponding K and Si elemental mapping images. (b) Fine K 2p XPS survey spectrum of the full-discharged electrode. (c) Comparison of Si 2p spectrum before and after the discharge process. (d) CV curves of c-silicene after activation tested at various scan rates from 0.2 to 4 mV s^{-1}. (e) Contribution ratios of the normalized capacitive and diffusion-controlled peaks from 0.2 to 4 mV s^{-1}. (f) The GITT curves and potassium-ion diffusion coefficients (D$_{K-ions}$) of the electrode.

further point to K $2p_{3/2}$ at 292.6 eV and K $2p_{1/2}$ at 295.4 eV in the fine K 2p spectrum respectively (Fig. 4b). The fine Si 2p spectrum shows that the peak located at 99.5 eV, which belongs to Si^0 (Si-Si), disappears in the full-discharged product. It is noted that a faint new peak appears at 98.8 eV and can be attributed to Si^-, that is, the generation of KSi (Fig. 4c).[20,21] As a silicide with negative valence, the surface of KSi may be unstable in air, so the slightly weaker peak intensity can be attributed to its extremely easy oxidation, which is similar to $CaSi_2$ or Mg_2Si.[22] The further evidence for the formation of KSi is consistent with the reaction mechanism indicated by SRXRD and TEM, which confirms the alloying reaction of c-silicene in the proposed KIB.

To further understand the ion transport process of the electrochemical reaction, the kinetics behavior of the proposed cell was studied. The potassium storage properties were examined using cyclic voltammetry (CV) at a scan rate of 0.2 mV s^{-1} in the potential range of 0.01–3.0 V (vs K^+/K). An overlapping shape is observed in the subsequent cycles, which proves that highly reversible potassiation/depotassiation processes occur in c-silicene (Fig. S8). Two plateau regions appeared during the first CV scan, and they were greatly weakened during the following cycle of CV scan, which is attributed to the generation of the solid electrolyte interphase (SEI) layer on the surface of the electrode material. Consecutive CV measurements at various scan rates was also carried out (Fig. 4d). The curves share nearly the same characteristics from 0.2 to 4 mV s^{-1}, suggesting the good reversibility of potassium storage at each scan rate. The peak current (i) response for the CV measurements at a scan rate (v) follows the equation:

$$i = av^b \qquad (1)$$

where a and b are variables. Diffusion-controlled behavior dominates when the b-value calculated from Eq. (1) approaches 0.5, and the surface-driven behavior dominates when the b-value is nearly 1.0. The calculated b-values are 0.83, and 0.86 for Peak 1, and Peak 2, respectively (Fig. S9), implying fast capacitive-dominant behavior. According to Dunn's method,[23] the surface process contribution at a fixed rate can be further quantitatively differentiated, separating the specific contribution from a surface-driven process (k_1v) and a diffusion-controlled process ($k_2v^{1/2}$), as shown in the following equation:

$$i(v) = k_1v + k_2v^{1/2} \qquad (2)$$

where k_1 and k_2 are constants. Fig. 4e displays the separate contributions of the surface and bulk charge processes at scan rates from 0.2 mV s^{-1} to 4 mV s^{-1}, with the calculated capacitive charges increasing from 51% to 83% of the total charge. The galvanostatic intermittent titration technique (GITT) was employed to probe the ion diffusion coefficient of potassium-ions in c-silicene (Fig. 4f). It can be observed that D_{K-ions} decreases slightly and varies from 8.66×10^{-8} to 7.21×10^{-9} cm^2 s^{-1} and 7.59×10^{-8} to 1.74×10^{-8} cm^2 s^{-1} over the entire discharge/charge progress for insertion and extraction, respectively. This ion diffusion kinetics proposed here suggest that c-silicene endow fast ion migration, leading to effective reaction ignition.

Furthermore, the electrochemical performance of c-silicene in potassium-ion battery is evaluated in coin cells using potassium metal as the counter electrode (Fig. S10). The initial cycling behavior of the K//c-silicene battery is shown in Fig. 5a, and the first three charge/discharge curves at a current density of 50 mA g^{-1} maintain a similar profile without obvious plateau regions. The c-silicene anode possesses an initial discharge capacity of 617.5 mA h g^{-1} and cycle for more than 50 cycles with reversible capacity of ~ 110 mA h g^{-1} (Fig. 5b). The irreversible capacity in the first cycle results in an initial Coulombic efficiency (CE) of 33% and rapidly grows to ~ 98% during the following cycles, suggesting a highly reversible potassiation/depotassiation process. It is generally accepted that the initial irreversible capacity can be ascribed to the formation of SEI layers and may be facilitated by the high specific surface area of silicene.[24] The rate capability was also measured to check the abuse tolerance at various current densities. As shown in Fig. 5c, the c-silicene anode showed a stable capacity of 180.1 mA h g^{-1} at 10 mA g^{-1}, and further demonstrated an adequate discharging capacity such as 105 mA h g^{-1} at 50 mA g^{-1} and 60 mA h g^{-1} at 500 mA g^{-1}, and the corresponding charge/discharge profiles maintain the same shape (Fig. S11b). The ultra-thin lamellar morphology of c-silicene probably avoids deeper ion diffusion, thereby decreasing the transport distance and accelerating the potassiation/depotassiation kinetics although this is originally difficult to react.[14]

Subsequently, the long-term cycling tolerance of c-silicene, which is an intractable problem for silicon-based anodes, was further examined. As shown in Fig. 5d, an enhanced cycle stability is achieved after 3000 cycles at a current density of 500 mA g^{-1} without visible capacity fading (capacity retention ~ 100%), and CE is maintained above 99.4%. The

Fig. 5. Electrochemical evaluation of the c-silicene electrode used in half and full KIBs. (a) Initial three discharge/charge curves at a current density of 50 mA g^{-1}. (b) Cycling performance at a current density of 50 mA g^{-1}. (c) Rate performance of c-silicene with rates ranging from 10 to 5000 mA g^{-1}. (d) Long-term cycling performance at a high current density of 500 mA g^{-1}. (e) Schematic diagram of full KIB configuration. (f) GCD curves of K//c-silicene (capacity is calculated based on c-silicene), K//PBA (capacity is calculated based on PBA), and c-silicene//PBA full KIB (capacity is calculated based on c-silicene) after activation. (g) Cycling performance of full KIB at a current density of 50 mA g^{-1}. Insert: GCD curves of full KIB after different cycles.

increased capacity with the number of cycles can be ascribed to the gradual activation process of electrode along with the continuous perfection of the SEI layer after long cycles. The two-dimensional graphene-like structure also alleviates the pulverization of the electrode, implying enhanced cycling stability of c-silicene with superior self-recoverability. For comparison, the electrode without c-silicene was also measured in a KIB to eliminate the contribution of the carbon black additive, and the obtained no-silicene capacity contribution is normalized as ~ 11 mA h g^{-1} (Fig. S12), further specifying the authenticity of the capacity of c-silicene. As proof of the suitable anode application of KIBs, a full c-silicene//Prussian blue analogue (PBA) KIB was assembled. As shown in the Fig. 5e, PBA as discharged $K_{0.22}Fe(Fe(CN)_6)$ is used as the cathode to increase the operating voltage range of the proposed battery. GCD curves show that the full battery can stably operate between 1.2 V and 3.2 V (Fig. 5f). The full KIB further delivers a reversible capacity of 107 mA h g^{-1} after cycling up to more than 50 cycles at 50 mA h g^{-1} (Fig. 5g, calculation based on silicene loading), indicating remarkable cycling stability and the compatibility application of c-silicene in potassium-ions alloying storage.

4. Conclusions

In summary, we report a c-silicene anode that shows highly reversible insertion/exaction process and enhanced electrochemical stability in KIBs. The large specific surface area and expanded interplanar spacing provide abundant space for potassium-ions storage, and the ultra-thin monatomic lamellar morphology shortens the diffusion distance of ions and indicates fast kinetics. The in situ SRXRD demonstrates the effective insertion/extraction behavior of potassium-ions, and the TEM and SEM-EDS measurements further confirmed that KSi formed in the discharge process. The c-silicene anode presented an adequate capacity of 180.1 mA h g^{-1}, high Coulombic efficiency (greater than 99.4%) and stability (greater than 3000 cycles). Given the long-standing viewpoint of the inertia of silicon anodes in potassium-ion storage, this encouraging result may open up a new way for the development of silicon electrodes as a promising energy storage technology for KIBs.

Declaration of Competing Interest

The authors declare that they have no known competing financial interests or personal relationships that could have appeared to influence the work reported in this paper.

Acknowledgements

Appendix A. Supplementary data

Supplementary data to this article can be found online at https://doi.org/10.1016/j.cej.2022.134961.

References

[1] X. Hua, A.S. Eggeman, E. Castillo-Martinez, R. Robert, H.S. Geddes, Z. Lu, C. J. Pickard, W. Meng, K.M. Wiaderek, N. Pereira, G.G. Amatucci, P.A. Midgley, K. W. Chapman, U. Steiner, A.L. Goodwin, C.P. Grey, Revisiting metal fluorides as lithium-ion battery cathodes, Nat. Mater. 20 (2021) 841–850, https://doi.org/10.1038/s41563-020-00893-1.

[2] J. Holoubek, H. Liu, Z. Wu, Y. Yin, X. Xing, G. Cai, S. Yu, H. Zhou, T.A. Pascal, Z. Chen, P. Liu, Tailoring Electrolyte Solvation for Li Metal Batteries Cycled at Ultra-Low Temperature, Nat. Energy (2021 (2021),) pp, https://doi.org/10.1038/s41560-021-00783-z.

[3] Y.H. Sun, D.M. Zhu, Z.F. Liang, Y.X. Zhao, W.F. Tian, X.C. Ren, J. Wang, X.Y. Li, Y. Gao, W. Wen, Y.B. Huang, X.L. Li, R.Z. Tai, Facile renewable synthesis of nitrogen/oxygen co-doped graphene-like carbon nanocages as general lithium-ion and potassium-ion battery anodes, Carbon 167 (2020) 685–695, https://doi.org/10.1016/j.carbon.2020.06.046.

[4] X.C. Ren, Y.X. Zhao, Q.W. Li, F. Cheng, W. Wen, L.L. Zhang, Y.B. Huang, X.H. Xia, X.L. Li, D.M. Zhu, K.F. Huo, R.Z. Tai, A novel multielement nanocomposite with ultrahigh rate capacity and durable performance for sodium-ion battery anodes, J. Mater. Chem. A 8 (2020) 11598–11606, https://doi.org/10.1039/d0ta04349d.

[5] S.S. Fedotov, N.D. Luchinin, D.A. Aksyonov, A.V. Morozov, S.V. Ryazantsev, M. Gaboardi, J.R. Plaisier, K.J. Stevenson, A.M. Abakumov, E.V. Antipov, Titanium-based potassium-ion battery positive electrode with extraordinarily high redox potential, Nat. Commun. 11 (2020) 1484, https://doi.org/10.1038/s41467-020-15244-6.

[6] Y. Wang, Z. Wang, Y. Chen, H. Zhang, M. Yousaf, H. Wu, M. Zou, A. Cao, R.P. S. Han, Hyperporous Sponge Interconnected by Hierarchical Carbon Nanotubes as a High-Performance Potassium-Ion Battery Anode, Adv. Mater. 30 (2018), e1802074, https://doi.org/10.1002/adma.201802074.

[7] J. Ryu, D. Hong, S. Choi, S. Park, Synthesis of Ultrathin Si Nanosheets from Natural Clays for Lithium-Ion Battery Anodes, ACS Nano 10 (2016) 2843–2851, https://doi.org/10.1021/acsnano.5b07977.

[8] C. Zeng, F. Xie, X. Yang, M. Jaroniec, L. Zhang, S.Z. Qiao, Ultrathin Titanate Nanosheets/Graphene Films Derived from Confined Transformation for Excellent Na/K Ion Storage, Angew. Chem. Int. Ed. Engl. 57 (2018) 8540–8544, https://doi.org/10.1002/anie.201803511.

[9] I. Sultana, M.M. Rahman, Y. Chen, A.M. Glushenkov, Potassium-Ion Battery Anode Materials Operating through the Alloying-Dealloying Reaction Mechanism, Adv. Funct. Mater. 28 (2018) 1703857, https://doi.org/10.1002/adfm.201703857.

[10] A.Y. Galashev, A.S. Vorob'ev, Physical properties of silicene electrodes for Li-, Na-, Mg-, and K-ion batteries, J. Solid State Electr. 22 (2018) 3383–3391, https://doi.org/10.1007/s10008-018-4050-8.

[11] R. Nesper, The Zintl-Klemm Concept - A Historical Survey, Z. Anorg. Allg. Chem. 640 (2014) 2639–2648, https://doi.org/10.1002/zaac.201400403.

[12] L.C. Loaiza, L. Monconduit, V. Seznec, Si and Ge-Based Anode Materials for Li-, Na-, and K-Ion Batteries: A Perspective from Structure to Electrochemical Mechanism, Small 16 (2020), e1905260, https://doi.org/10.1002/smll.201905260.

[13] J. Liu, Y. Yang, P. Lyu, P. Nachtigall, Y. Xu, Few-Layer Silicene Nanosheets with Superior Lithium-Storage Properties, Adv. Mater. 30 (2018) 1800838, https://doi.org/10.1002/adma.201800838.

[14] Y.L. Xu, E. Swaans, S. Basak, H.W. Zandbergen, D.M. Borsa, F.M. Mulder, Reversible Na-Ion Uptake in Si Nanoparticles, Adv. Energy Mater. 6 (2016) 1501436, https://doi.org/10.1002/aenm.201501436.

[15] M. Nematzadeh, A. Massoudi, M. Nangir, Optimization of silicene oxidation as lithium-ion battery anode, Mater. Today-Proc. 42 (2021) 1588–1591, https://doi.org/10.1016/j.matpr.2020.03.210.

[16] H. Lin, W. Qiu, J. Liu, L. Yu, S. Gao, H. Yao, Y. Chen, J. Shi, Silicene: Wet-Chemical Exfoliation Synthesis and Biodegradable Tumor Nanomedicine, Adv. Mater. 31 (2019), e1903013, https://doi.org/10.1002/adma.201903013.

[17] E. Cinquanta, E. Scalise, D. Chiappe, C. Grazianetti, B. van den Broek, M. Houssa, M. Fanciulli, A. Molle, Getting through the Nature of Silicene: An sp^2–sp^3 Two-Dimensional Silicon Nanosheet, J. Phys. Chem. C 117 (2013) 16719–16724, https://doi.org/10.1021/jp405642g.

[18] L. Tao, E. Cinquanta, D. Chiappe, C. Grazianetti, M. Fanciulli, M. Dubey, A. Molle, D. Akinwande, Silicene field-effect transistors operating at room temperature, Nat. Nanotechnol. 10 (2015) 227–231, https://doi.org/10.1038/nnano.2014.325.

[19] E. Busmann, **Das Verhalten der Alkalimetalle zu Halbmetallen. X. Die Kristallstrukturen von KSi, RbSi, CsSi, KGe, RbGe und CsGe.** Z. Anorg. Allg. Chem., 313 (1961), pp. 90-106. 10.1002/zaac.19613130108.

[20] F. Esaka, T. Nojima, H. Udono, M. Magara, H. Yamamoto, Non-destructive depth analysis of the surface oxide layer on Mg$_2$Si with XPS and XAS, Surf. Interface Anal. 48 (2016) 432–435, https://doi.org/10.1002/sia.5939.

[21] H. Nakano, S. Yamanaka, M. Hattori, Reactivity of Rf Magnetron Sputtered CaSi$_2$ Film, Solid State Ionics 53 (1992) 635–640, https://doi.org/10.1016/0167-2738(92)90440-Z.

[22] M.R.J. van Buuren, F. Voermans, H. vanKempen, Bonding in Mg$_2$Si Studied with X-ray Photoelectron Spectroscopy, J. Phys. Chem. 99 (2002) 9519–9522, https://doi.org/10.1021/j100023a033.

[23] V. Augustyn, J. Come, M.A. Lowe, J.W. Kim, P.L. Taberna, S.H. Tolbert, H. D. Abruna, P. Simon, B. Dunn, High-rate electrochemical energy storage through Li$^+$ intercalation pseudocapacitance, Nat. Mater. 12 (2013) 518–522, https://doi.org/10.1038/nmat3601.

[24] S. Zhao, Z. Wang, Y. He, H. Jiang, Y.W. Harn, X. Liu, C. Su, H. Jin, Y. Li, S. Wang, Q. Shen, Z. Lin, A Robust Route to Co$_2$(OH)$_2$CO$_3$ Ultrathin Nanosheets with Superior Lithium Storage Capability Templated by Aspartic Acid-Functionalized Graphene Oxide, Adv. Energy Mater. (2019), https://doi.org/10.1002/aenm.201901093.